Electronic transition, ferroelectric and thermoelectric properties of bismuth pyrostannate $Bi_2(Sn_{0.85}Cr_{0.15})_2O_7$

S.S. Aplesnin[a,b], L.V. Udod[a,b,*], M.N. Sitnikov[b]

[a] *Kirensky Institute of Physics, Federal Research Center KSC SB RAS, Akademgorodok, 50, Krasnoyarsk 660036, Russia*
[b] *Siberian State Aerospace University M. F. Reshetnev, Krasnoyarsky Rabochy Av. 31, 660014 Krasnoyarsk, Russia*

ARTICLE INFO

ABSTRACT

The ferroelectric properties of bismuth pyrostannate $Bi_2(Sn_{0.85}Cr_{0.15})_2O_7$ in the high-temperature region are established. The linear thermal expansion coefficient, electrical resistance, impedance, $I-V$ characteristics, capacitance, loss-angle tangent, charge, and thermopower of the investigated material are measured in the temperature range of $300-700$ K at frequencies of 10^2-10^6 Hz. Anomalies of the thermal expansion coefficient and hodograph spectrum variation in the region of polymorphic phase transitions are observed. The high resistance and change of the hopping conductivity for the tunnel-emission are found. The hysteresis in the electric field dependence of polarization is established. The change in the thermopower sign with temperature is revealed. The obtained experimental data are explained in the framework of the model of migration polarization by charged chromium ions.

1. Introduction

At present time, the materials with specified properties, including magnets, ferroelectrics, and pyroelectrics, have been intensively studied. The optical and electrical properties of these materials are important for application in optical storage devices [1], sensors [2] and capacitors operating in a wide temperature range, pyroelectric detectors, [3] and nonlinear optical devices [4]. The electric polarization of ferroelectric materials can be switched between several states by an external electric field. This feature is promising for application in electronics and information technologies for data recording. The available ferroelectric materials are characterized by the high thermal and chemical stability and fast electromechanical response. The ferroelectric properties of crystals are determined by their structure and the presence of certain functional groups or ion environment in their lattice. The five mechanisms that are considered to be responsible for ferroelectricity are:

 (i) displacement of the electron density of an unshared electron pair typical of the $BiFeO_3$-type perovskites [5];
 (ii) charge ordering [6];
(iii) "geometrical" ferroelectricity, which is the most similar to the classical model of displacements of the charges localized on ions [7]; and
 (iv) two types of "spin" (magnetic order-induced) ferroelectricity types,

including nonrelativistic one typical of collinear magnets and relativistic one observed in chiral magnets [8].

The variation in spontaneous polarization P_s with temperature induces the pyroelectric current. The change in P_s and occurrence of electric charges on crystal faces are caused by minor temperature variations of the polar structural distortions or by changes in the charge ordering. Such changes occur for the time similar in the order of magnitude to the atomic oscillation period, which ensures a small lag time of the spontaneous polarization variation with temperature.

Linear pyroelectric crystals are characterized by the linear field dependence of polarization $P(E)$, do not undergo phase transitions, and demonstrate the spontaneous polarization over the entire temperature range of their existence. In contrast to linear nonpolar dielectrics, in linear pyroelectrics the $P(E)$ dependence passes through a nonzero value at E = 0. The pyroelectric coefficient of linear pyroelectrics is usually smaller than that of ferroelectrics [9]. The materials characterized by the pyroelectric effect can also be used as sensors and power sources for microelectronic applications [10].

The above-mentioned characteristics can be obtained in bismuth pyrostannate $Bi_2Sn_2O_7$ with the pyrochlore crystal structure, which exhibits a variety of properties, including the second optical harmonic generation. For instance, in cadmium pyroniobate $Cd_2Nb_2O_7$ the transition from the paraelectric cubic phase to pseudocubic one at $T_B = 205$ K is accompanied by a permittivity anomaly. In this case, the

spontaneous polarization occurs [11]. The effect is intensified by doping with iron ions [12]. In the $Bi_2Sn_2O_7$ compound, bismuth ions have an unshared electron pair and the absence of inversion center in the crystal can lead to the spontaneous polarization.

Substitution of the tin ions in $Bi_2Sn_2O_7$ by 3d metals (Me) will enhance the asymmetry of the Sn-O-Bi-O-Me bond and, consequently, increase the polarization. The replacement of tetravalent tin ions by trivalent chromium ones induces charge ordering, which results in the additional contribution to the polarization and intensification of the pyroelectric effect.

The aim of this study was to establish the ferroelectric properties and pyroelectric effect in bismuth pyrostannate $Bi_2(Sn_{0.85}Cr_{0.15})_2O_7$ doped with chromium ions in the high-temperature range.

2. Experimental

The $Bi_2(Sn_{0.85}Cr_{0.15})_2O_7$ compound was synthesized by the solid state reaction technique using the scheme:

$2(1-x)SnO_2 + 2xCrO_2 + Bi_2O_3 \rightarrow Bi_2(Sn_{1-x}Cr_x)_2O_7$, where $x = 0.15$.
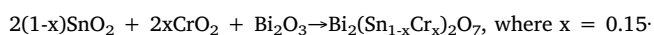
The initial substances were ultrapure Bi_2O_3, SnO_2, and Cr_2O_3 oxides. The initial oxide mixture was tableted, placed in a furnace, and exposed at temperatures from 700 to 950 °C for $8 - 24$ h.

At room temperature, the $Bi_2Sn_2O_7$ crystal structure represents a distorted pyrochlore one [13] and undergoes three polymorphic transitions [14,15]. The thermodynamically stable noncentrosymmetric monoclinic α-$Bi_2Sn_2O_7$ phase with sp. gr. $P1c1$, $\beta = 90.04$, and 176 crystallographically independent atoms is existed at temperatures of up to 137 °C [16]. The independent part of the cell contains 32 Bi^{3+} ions, 32 Sn^{4+} ions, and 112 O^{2-} ions (Fig. 1a). All the Bi^{3+} ions are

surrounded by eight oxygen ions and form a distorted cube; the Sn^{4+} ion is surrounded by six vertex-sharing oxygen ions forming a distorted octahedron. Each atom is displaced from the corresponding position in the ideal pyrochlore cubic structure; the distortion of the Sn-O sublattice is significantly smaller than that of Bi-O´. The average displacements from the ideal pyrochlore structure are 0.389, 0.104, 0.189, and 0.312 Å for Bi, Sn, O, and O´ respectively. The Sn atoms have a valence of $+4$ and electronic configuration $4d^1 5s^0$; the Bi atoms is a valence of $+3$ and electronic configuration $5d^{10}6s^2$. At the temperature corresponding to the first phase transition, the unit cell is distorted. The β-phase structure determined by neutron and synchrotron X-ray diffraction is cubic with sp. gr. $F\bar{4}3c(T_d^5)$ [17]. Above 680 °C, one more polymorphic transition to the γ phase with sp. gr. $Fd\bar{3}m$ occurs [18–20]. The transition $\alpha \rightarrow \beta$ at 135 °C is accompanied by the second harmonic generation [18].

The $Bi_2Sn_2O_7$ crystal structure consists of two mutually penetrating chains, Bi_2O' and SnO_6. In pyrochlores ($A_2B_2O_7$), BO_6 octahedra are arranged in zigzag chains in the (110) direction with a B-O-B bond angle of ~135°.

The structure of the synthesized $Bi_2(Sn_{0.85}Cr_{0.15})_2O_7$ samples (Fig. 1a) was analyzed on a Bruker D8 ADVANCE X-ray diffractometer with a VANTEC linear detector (CuK_α radiation) at room temperature. All the peaks in the XRD pattern, except for two weak impurity peaks of unknown phase, correspond to the monoclinic cell Pc in the $Bi_2Sn_2O_7$ α phase [16]. The Rietveld refinement was made using a TOPAS 4.2 program [21]. Coordinates of all 176 atoms were fixed, since the number of only 528 coordinates was comparable with the number of observed reflections. Nevertheless, even fixed atomic coordinates allowed us to describe correctly all the observed reflections and the refinement yielded small uncertainty factors (Fig. 1b). Since the atomic coordinates and heat parameters were not refined, their values can be borrowed from study [16]. The decrease in the cell volume upon substitution confirms that the $Bi_2(Sn_{0.85}Cr_{0.15})_2O_7$ composition is similar to the real chromium concentration, since the ionic radius IR(Cr^{3+}, CN = 6) = 0.615 Å is smaller than the radius of the substituted ion IR(Sn^{4+}, CN = 6) = 0.69 Å [22]. The Cr^{+3} ions occupy preferably the octahedral positions.

The electrical properties of $Bi_2(Sn_{0.85}Cr_{0.15})_2O_7$ were investigated by a four-probe technique on a 6517 V electrometer in the temperature range of 350–700 K. Impedance, capacitance, and loss-angle tangent were measured on an AM-3028 component analyzer in the frequency range of 0.1–1000 kHz at temperatures of 300–750 K. The pyroelectric current was measured with a Keithley 6517b electrometer upon continuous sample temperature variation between 300–800 K on the samples with electrodes deposited onto the opposite faces. The pyroelectric current was detected from the entire sample volume. The charge on the surface of a sample placed between plates of a capacitor with a mica spacer to avoid leakage currents was detected on a Keithley 6517b electrometer. The thermoelectric voltage on the opposite sample faces was measured with an Agilent Technologies 34410 A digital multimeter in the temperature range of 300–650 K. The linear thermal expansion coefficient was measured by ZFLA-3–11 strain gauge with a resistance of $R = 210 \Omega$. The relative difference between the strain gauge resistances on the sample (R_s) and on mica (R_m) with a thermal expansion coefficient of $3 \cdot 10^{-6} K^{-1}$ at fixed temperature $(R_s(T) – R_m(T))/(R_m(T) * T)$ corresponds to the thermal expansion coefficient of $Bi_2(Sn_{0.85}Cr_{0.15})_2O_7$.

3. Results and discussion

3.1. Structural and electrical properties

The structural phase transitions are accompanied by the variation in lattice parameters and, as rule, in the volume. At the temperature T = 380 K of the structural phase transition $\alpha - \beta$, the thermal expansion coefficient increases stepwise and has the minimum at T = 556 K
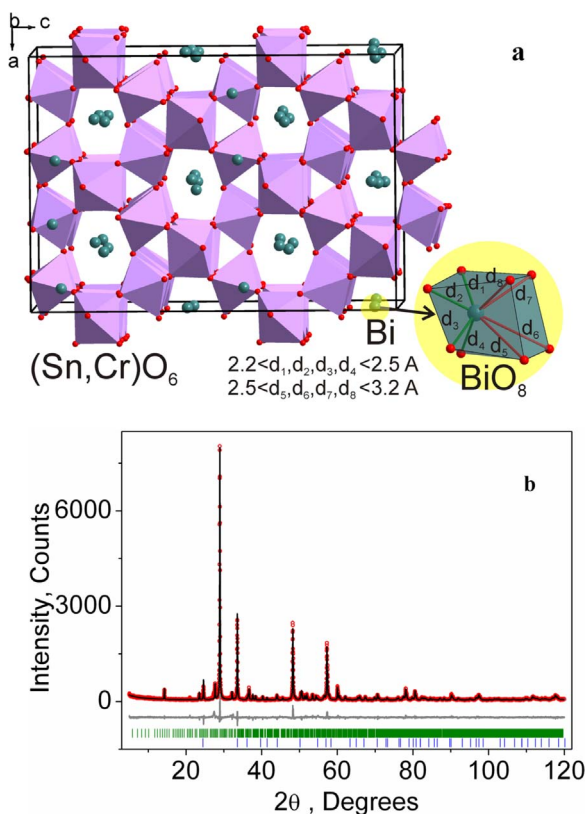
Fig. 1. (a) $Bi_2(Sn_{0.85}Cr_{0.15})_2O_7$ crystal structure. The BiO_8 fragment is shown separately. (b) Difference XRD pattern of $Bi_2(Sn_{0.85}Cr_{0.15})_2O_7$. The upper curve shows the experimental XRD pattern; the middle curve, the theoretical XRD pattern; and the lower curve, the difference between the theoretical and experimental XRD patterns.
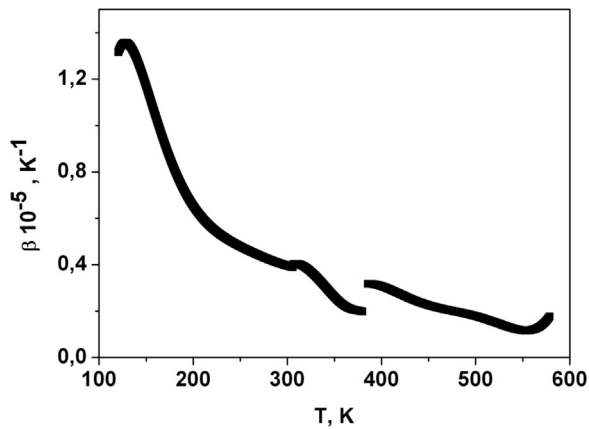
Fig. 2. Temperature dependence of the thermal expansion coefficient of $Bi_2(Sn_{0.85}Cr_{0.15})_2O_7$.

(Fig. 2). Possibly, the compound under study undergoes one more structural transition at T = 130 K. The sharp increase of absorption intensity at frequency ω = 632 cm^{-1} was observed at temperature T = 125 K for bismuth pyrostannate $Bi_2(Sn_{0.95}Cr_{0.05})_2O_7$ [23]. Here, the IR absorption is attributed to the stretching oscillations of the Sn–O bond in the oxygen octahedron SnO_6 of the pyrochlore structure. A decrease in the thermal expansion coefficient with increasing temperature is indicative of weakening of the nonlinearity and lattice anharmonism.

The electrical resistance increases from $4.5 \cdot 10^{10}$ to $5 \cdot 10^{10}$ Ω upon heating at temperatures of 100–400 K. At the temperature T = 375 K of the structural transition α → β, the resistance sharply grows by 5%. The temperature dependence of the resistance has a broad maximum near T = 250 K, which was observed also in the $Bi_2Sn_2O_7$ sample [24]. The resistance growth results from rearrangement of the electronic structure at the structural phase transition.

We determine the conductivity mechanism and existence of in-homogeneous electronic states from the *I–V* characteristics of $Bi_2(Sn_{0.85}Cr_{0.15})_2O_7$, which were measured in external electric fields from −800 to 800 V/cm. As the temperature is increased, the shape of the *I(U)* curve changes. In the temperature range of charge ordering, the conductivity is described within the model of currents limited by the space charge using the Mott quadratic law [25,26]

$$j = \frac{9}{8}\tau_\mu \sigma_0 \mu \frac{U^2}{L^3}, \tag{1}$$

where *j* is the current density, τ_μ is the Maxwell relaxation time, σ_0 is the electrical conductivity in the bulk of the material in the absence of carrier injection, μ is the carrier mobility, *U* is the applied voltage, and *L* is the sample thickness. The experimental *I–V* characteristics in the logarithmic coordinates shown in Fig. 4a are described well by Eq. (1).

At temperatures above 400 K, the hysteresis of the *I–V* character-istics is observed, since the current at the increasing external electric field *dE/dt > 0* is larger than at the decreasing field *dE/dt < 0*. In the presence of polar regions, the external electric field tends to rotate polarization vector *P* parallel to the field, which will lead to a decrease in the internal electric field in the sample, $E = E_0 - \varepsilon_0 E'$, $E' = P/\varepsilon_0$ and, consequently, in the current density at a certain voltage. In a poly-crystal, the anisotropy axes are randomly oriented and the polarization can take two equilibrium values. As a result, the internal electric field decreases in the applied electric field and the hysteresi of the *I–V* characteristics is observed. The relative current difference $\Delta I/I = (I(dE/dt > 0) - I(dE/dt < 0))/I(dE/dt > 0)$ as a function of the field is pre-sented in Fig. 3c.

In the high-temperature region, starting from T = 450 K, the Pool–Frenkel conductivity prevails (Fig. 3b), at which a strong electric field applied to a sample changes the shape of potential barriers for carriers. This mechanism is characterized by linear portions in the
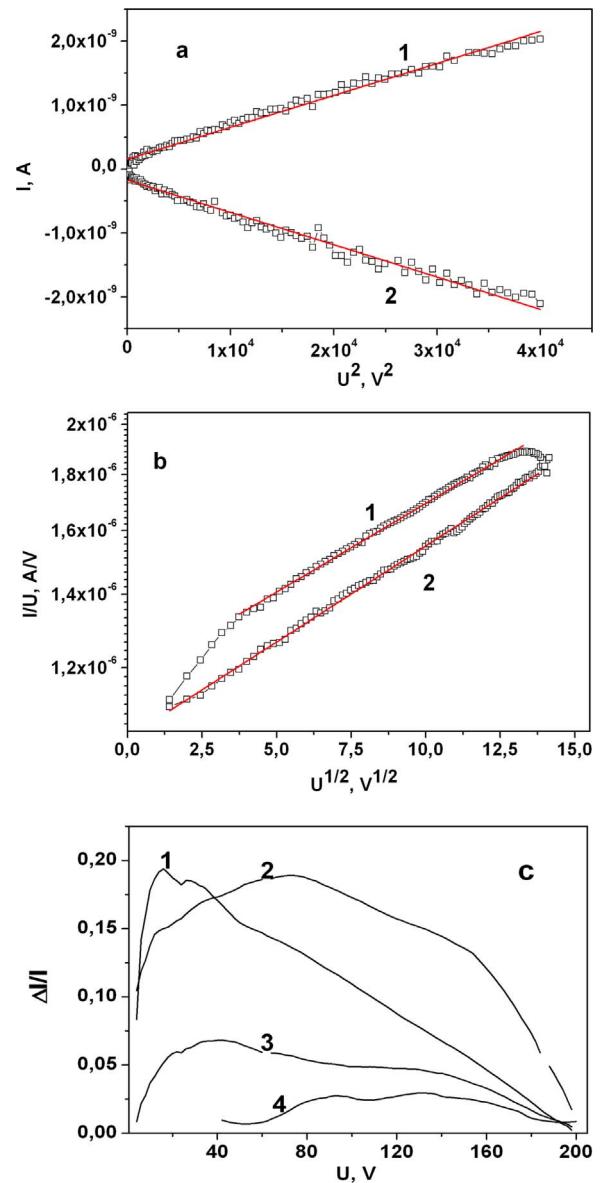

Fig. 3. *I–V* characteristics of $Bi_2(Sn_{0.85}Cr_{0.15})_2O_7$. (a) Dependence of the current on the squared applied voltage at T = 300 K. Curve *1* corresponds to the positive voltage, *2* - negative voltage. (b) Pool–Frenkel *I–V* characteristic measured at T = 600 K. Curve *1* - positive voltage, *2* -negative voltage. (c) Temperature dependence of the relative current difference $(I(dE/dt < 0) - I(dE/dt > 0))/I(dE/dt > 0)$ on the applied voltage. Curves *1, 2, 3,* and *4* correspond to temperatures of 450, 500, 550, and 600 K.

temperature dependences of the conductivity on the square root of applied voltage of different polarities, which is indicative of the con-tribution of carriers occurring due to the Pool–Frenkel emission to the current. In this case, the current depends exponentially on applied voltage and the exponent contains the square root of voltage [27–29].

$$I = e\mu n_0 \frac{U}{L} \exp\frac{\beta U^{1/2}}{kTL^{1/2}}, \tag{2}$$

where *e* is the elementary charge, μ is the carrier mobility, n_0 is the electron concentration in the conduction band in zero field, *U* is the applied voltage, *L* is the sample thickness, *k* is the

Boltzmann constant, β is the Pool–Frenkel constant, $\beta = \left(\frac{e^3}{\pi\varepsilon\varepsilon_0}\right)^{1/2}$, ε_0 is the permittivity of

vacuum, and ε is the permittivity of a semiconductor. The linearity of the plots in the *ln(I/U)* dependence from $U^{1/2}$ in the Pool–Frenkel coordinates (Fig. 3c) indicates that carrier transport in
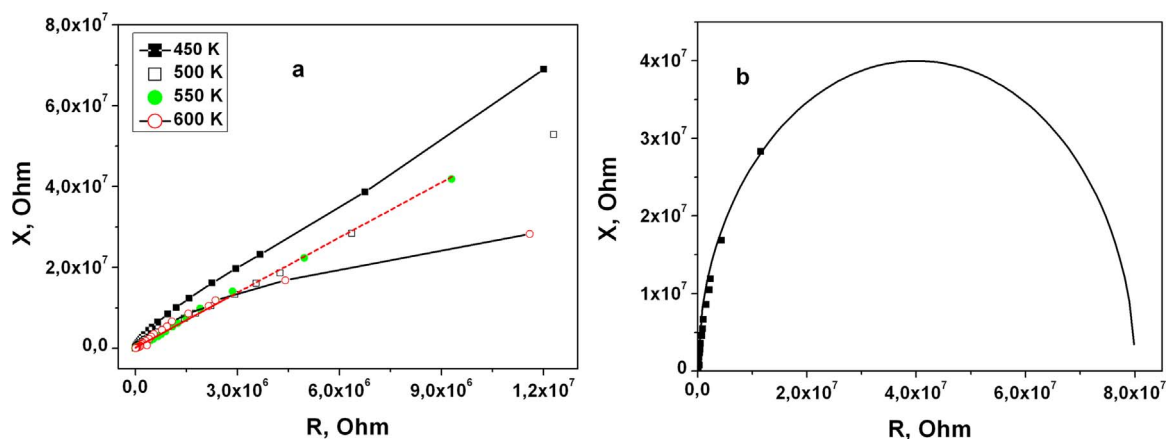
Fig. 4. Temperature dependence of the impedance spectra of $Bi_2(Sn_{0.85}Cr_{0.15})_2O_7$. (a) Impedance spectra presented at temperatures of 450, 500, 550, and 600 K. The dashed line corresponds to 550 K. (b) Equivalent circuit of the parallel connection of a resistance of R = $8 \cdot 10^7$ Ω and a capacitance of C = $3 \cdot 10^{-8}$ F of $Bi_2(Sn_{0.85}Cr_{0.15})_2O_7$ at T = 600 K.

$Bi_2(Sn_{0.85}Cr_{0.15})_2O_7$ is implemented mainly via hopping conductivity and tunnel electron emission. The heterovalence of Sn and Cr leads to the occurrence of an unpaired electron in the potential well created by chromium ions. Under the action of the external electric field, this electron tunnels between chromium ions.

The capacitive and inductive carrier contributions in the samples can be estimated by impedance spectroscopy. Fig. 4 shows the $Bi_2(Sn_{0.85}Cr_{0.15})_2O_7$ hodograph at some temperatures in the frequency range of $10^2 - 10^6$ Hz. The linear X(R) dependence reflects the diffusion process and is described by the Warburg impedance [30–32]. Possibly, the diffusion is the result of electrons hopping over the nearest sites [33]. The impedance hodograph above 550 K is approximated by an equivalent circuit with parallel connection of the capacitance and resistance at a relaxation time of $\tau = RC = 2.4$ s (Fig. 4b).

In the $Bi_2(Sn_{0.85}Cr_{0.15})_2O_7$ β phase, the active resistance has a broad maximum (Fig. 5a), whose temperature shifts from T = 590 K at a frequency of 1 kHz toward higher temperatures in accordance with the logarithmic law $T_m = 100 + 94 \log(\omega)$. Below the temperature of the transition α→β, the reactive resistance (Fig. 5b) is caused by only the capacitive contribution and the frequency dependence is described by the power law $X = A/\omega^n$. In the noncentrosymmetric cubic phase, the exponent decreases from unity to n = 0.8, which is indicative of addition of the inductive contribution from carriers. The impedance monotonically decreases with heating as a result of capacitance growth.

3.2. Permittivity

The spectral and temperature dependences of the permittivities can be used to establish the dipole electric moment and determine its characteristics, even when we speak about the local dipole moment in small clusters without long-range order. In addition, the dielectric properties are given information about charge transport and charge ordering.

The temperature dependences of the permittivity for several frequencies are presented in Fig. 6. The real part of the permittivity (Fig. 6a) has an inflection point and the imaginary part (Fig. 6b) has the maximum, whose temperature shifts to the high-temperature region with increasing frequency from T = 512 K at ω = 1 kHz to T = 700 K at ω = 300 kHz. Upon further heating, the real and imaginary parts of the permittivity sharply increase and depend on frequency.

In the β phase, there is the polarization caused by the electron migration in crystal grain and localization on the grain boundary. Localization of electrons of chromium ions leads to the permittivity maxima.

The frequency characteristics of the complex permittivity in the range from 1 to 1000 kHz are presented in Fig. 7. The dielectric relaxation cannot be described by a simple exponential law with one activation energy. In the most general case, the dipole moment relaxation can be described in terms of continuous distribution of relaxation times, when a system contains a set of local minima and potential barriers between them. A series of alternating relaxation processes occur in the system. This slows down the relaxation and leads
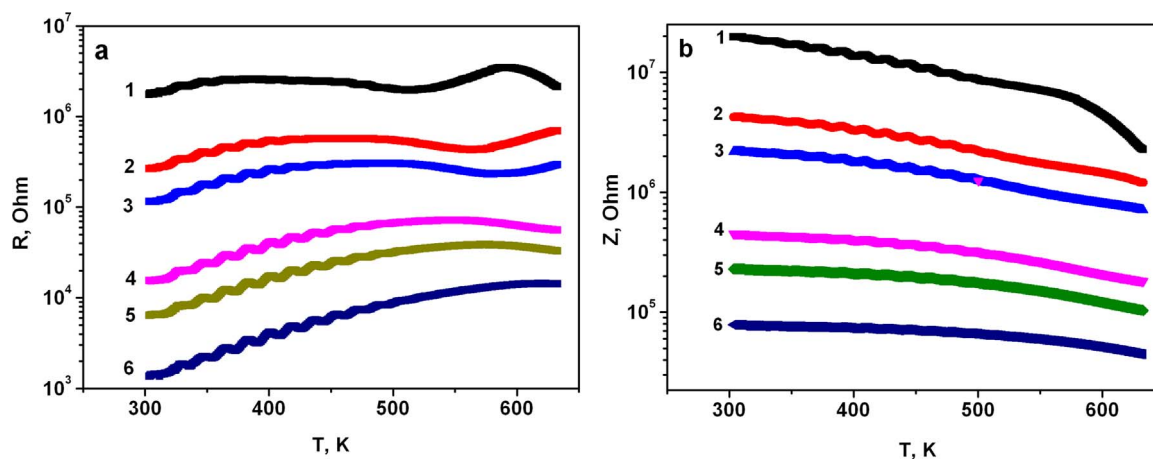

Fig. 5. Temperature and frequency dependence of the resistance of $Bi_2(Sn_{0.85}Cr_{0.15})_2O_7$: (a) active resistance and (b) reactive resistance. Curve *1* corresponds to 1 kHz, *2*–5 kHz, *3*–10 kHz, *4*–50 kHz, *5*–100 kHz, *6*–300 kHz.
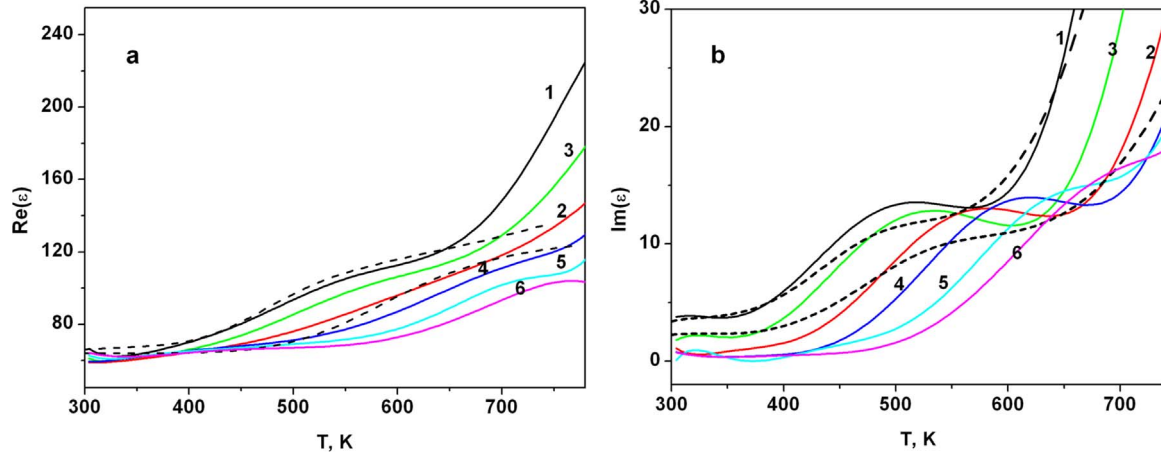
Fig. 6. Temperature dependence of the permittivity of $Bi_2(Sn_{0.85}Cr_{0.15})_2O_7$ at different frequencies: (a) real part and (b) imaginary part. Curve *1* corresponds to 1 kHz, *2* - 5 kHz, *3* - 10 kHz, *4* - 50 kHz, *5* - 100 kHz, *6* - 300 kHz. The $Re(\varepsilon)$ and $Im(\varepsilon)$ functions calculated using the Debye model at frequencies 1 kHz and 5 kHz (dashed lines).

to the transformation of the Debye exponent to the dependences descending with time at a lower rate. To describe qualitatively the permittivity, we approximate the relaxation time spectrum by two times τ_1 and τ_2 expressed by the Arrhenius function $\tau = \tau_0 exp\,(\Delta E/kT)$, where ΔE is the activation energy.

We write the permittivity using the Debye model

$$Re(\varepsilon) = \varepsilon_0 + \chi_0/(1 + (\omega\tau_1)^2) + \chi_0/(1 + (\omega\tau_2)^2), \quad (3)$$

$$Im(\varepsilon) = \chi_0\omega\tau_1/(1 + (\omega\tau_1)^2) + \chi_0\omega\tau_2/(1 + (\omega\tau_2)^2) + \sigma/\omega\varepsilon_0, \quad (4)$$

where ε_0 is the frequency–independent contribution to the permittivity, χ_0 is the static susceptibility of dipoles, ω is the frequency, $\sigma = \sigma_0 exp\,(-\Delta E_c/kT)$ is the sample conductivity, and ΔE_c is the carrier activation energy. The permittivity of $Bi_2(Sn_{0.85}Sn_{0.15})_2O_7$ is described satisfactorily by function (3, 4) (dashed lines in Figs. 6 and 7); the activation energies are $\Delta E_1 = 0.26$ eV, $\Delta E_2 = 0.15$ eV, and $\Delta E_c = 0.52$ eV.

3.3. Polarization and thermopower

Field dependences of the electric polarization vector of $Bi_2(Sn_{0.85}Cr_{0.15})_2O_7$ were obtained by measuring the surface charge as a function of electric field at temperatures of T = 300, 350, 400, 450, 500, and 550 K. At these temperatures, except for 550 K, we observed the hysteresis loop, which is indicative of the ferroelectric properties. Below a transition temperature of 370 K, the *P(E)* hysteresis loop is symmetric and above it shifts along the polarization axis. The loop shift increases upon heating and arises from thermal emission current j_t and

pyroelectric current j_p:

$$Q = 2P_S S + S \int j_p\,dt + S \int j_t\,dt, \quad (5)$$

where P_S is the spontaneous polarization and S is the capacitor area. Fig. 8a presents field dependences of polarization after subtraction of the thermal emission and pyroelectric currents.

The remanent polarization P_r at E = 0 increases with temperature (Fig. 8b) and has a sevenfold jump at the structural transition with increasing P_r. Polarization is due to the filling of vacant electronic states of N_v on the surface of the crystallite. These states are filled with electrons from the impurity ions of chromium $N_v = N_0 exp(-\Delta E_2/kT)$ at heating. The number of electrons on the surface of the crystallite increases and amounts to $N_s = N_{s0} + N_v$, where N_{s0} is the number of electrons on the surface at T = 0. The electron polarization of the crystallite disappears when the electrons are delocalized on the surface and the charge is formed near the contacts, $\sigma = evN_c$, where N_c is the electron concentration in the near-contact region, and v is the velocity of the current carriers. Let us estimate the functional dependence of the polarization on the temperature:

$$P = A(vN_c - N_s) = AN_s\left(\frac{vN_c}{N_s}-1\right) = a(1+b\cdot \exp\,(-\frac{\Delta E_2}{kT})(1$$
$$-cT^{3/2}\cdot \exp\,(-\frac{\Delta E_c}{kT})/(1+b\cdot \exp\left(-\frac{\Delta E_2}{kT}\right), \quad (6)$$

where a, b, c are parameters that do not depend on temperature. In Fig. 8, the fitting function (6) describes satisfactorily the experimental
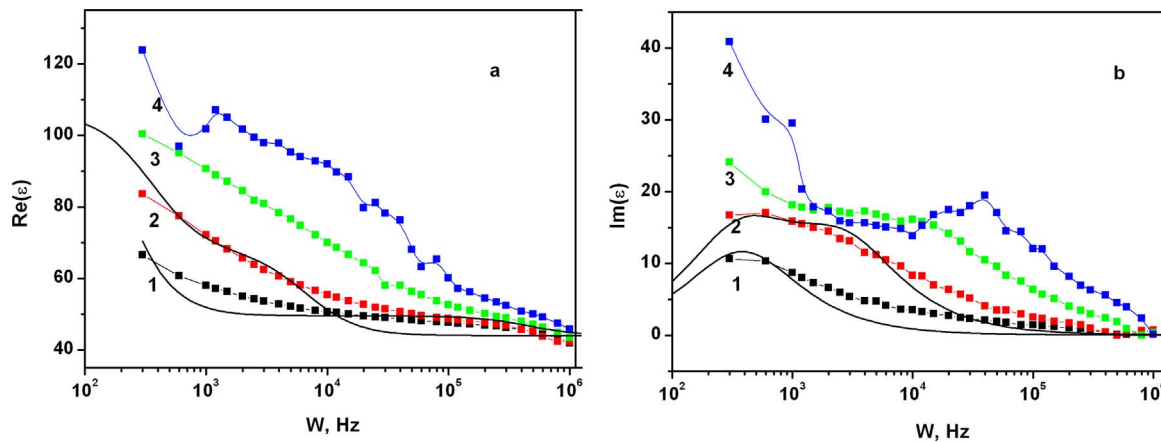

Fig. 7. Frequency dependence of the permittivity of $Bi_2(Sn_{0.85}Cr_{0.15})_2O_7$ at different temperatures: (a) real part and (b) imaginary part. Curve *1* corresponds to 450 K; *2* - 500 K; *3* - 550 K, and *4* - 600 K. Frequency dependences $Re(\varepsilon)$ and $Im(\varepsilon)$ calculated using the Debye model at T = 450 and 500 K (solid lines).
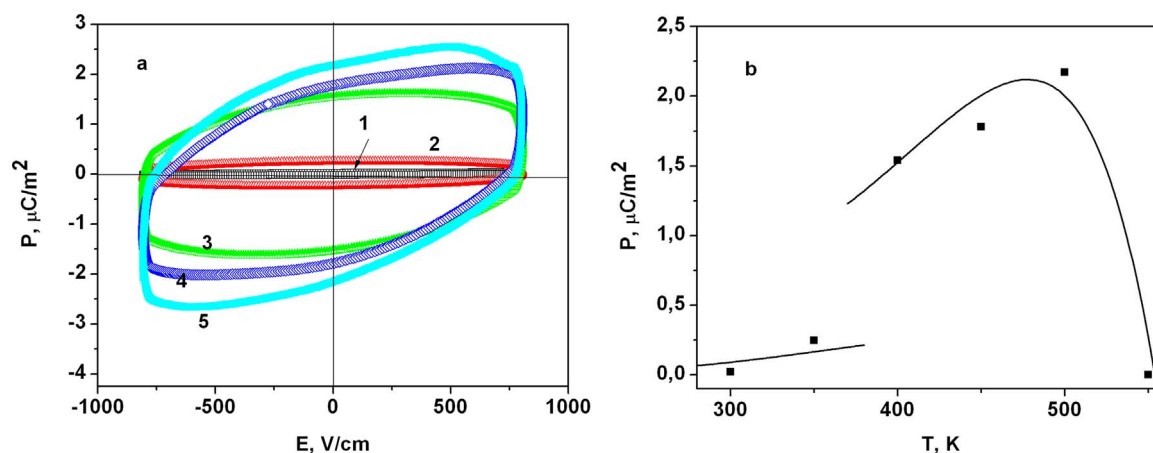
Fig. 8. (a) Dependence of the polarization of $Bi_2(Sn_{0.85}Cr_{0.15})_2O_7$ versus electric field at different temperatures: curve *1* corresponds to 300 K, *2* – 350 K, *3* – 400 K, *4* – 450 K, *5* - 500 K. (b) Temperature dependence of the remanent polarization of $Bi_2(Sn_{0.85}Cr_{0.15})_2O_7$.

results. The activation energy $\Delta E_2 = 0.15$ eV in the cubic phase coincides with the energy in the Arrhenius law for dielectric relaxation.

To extract the polarization from (6), we measured the current in zero electric field. Fig. 9 shows the temperature dependence of the current. The current grows exponentially above 460 K and is described well by the dependence of $lg(I)$ on 1000/T in the temperature range of 470–750 K with an activation energy of $\Delta E = 1.12$ eV. The current in zero electric field is caused by the pyroelectric effect and thermopower.

In addition to the primary pyroelectric effect, one can observe the polarization drop caused by heat expansion of bismuth pyrostannate. All pyroelectrics are piezoelectrics; therefore, heat expansion by means of the direct piezoelectric effect changes the polarization. This is the secondary pyroelectric effect. The pyroelectric current can be measured by a dynamic technique. The existence of the pyroelectric current is confirmed by the thermopower.

Fig. 10 shows the temperature dependence of the thermopower coefficient in the range of 300–650 K. The thermopower sign changes from negative to positive at a temperature of T = 525 K near the temperature of disappearance of the remanent polarization, which indicates the transition to the hole conductivity. The maximum thermopower is attained at 627 K. The thermoelectric current changes its sign upon heating and the current in zero external field increases exponentially with an increase in temperature.

The coefficient of efficiency, calculated from the relation $ZT = \alpha^2 T / k\rho$, where α is the Seebeck coefficient, ρ is the electrical resistivity, k is the thermal conductivity, and T is the absolute temperature is two orders of magnitude lower than in the binary and ternary compounds formed by IV (Ge, Sn, Pb) and group V (Sb, Bi) elements
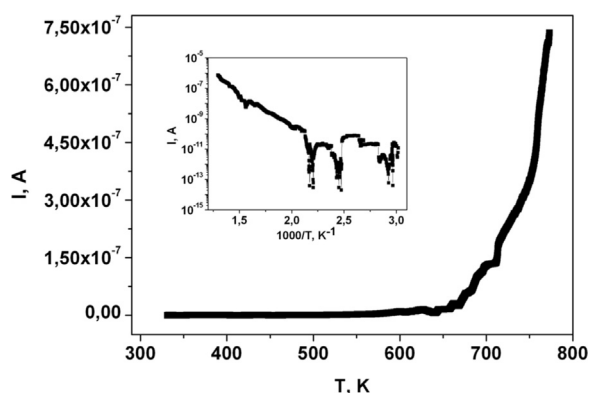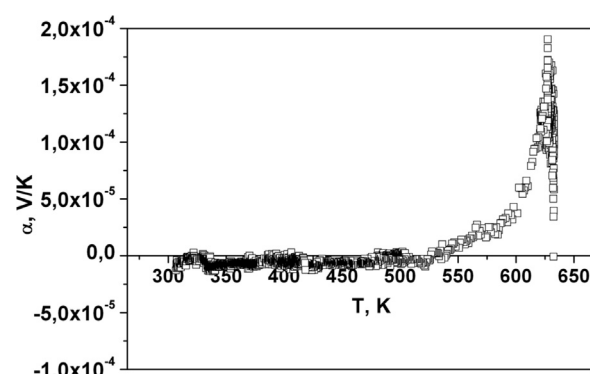

Fig. 10. Temperature dependence of the thermopower coefficient of $Bi_2(Sn_{0.85}Cr_{0.15})_2O_7$.

that related to well-known popular thermoelectric materials [34–41]. The thermoelectric properties of these compounds are highly dependent on the current carrier concentration, the temperature, and the preparation technique. These compounds are possessed high Seebeck coefficient, low electrical resistivity, and low thermal conductivity values [35].

4. Conclusions

We synthesized a new single-phase compound, bismuth pyrostannate, substituted by chromium with the monoclinic symmetry without inversion center. We found a jump in the linear thermal expansion coefficient of the lattice at the polymorphic transition from the monoclinic to cubic phase and minimum at the temperature of disappearance of spontaneous polarization. The electronic transition with the variation in the conductivity type from hopping to Pool–Frenkel emission is found.

The frequency dependences of the permittivity are described satisfactorily by the exponential law of dipole relaxation with two activation energies. The permittivity and dielectric loss decrease with increasing frequency. We established the polarization hysteresis upon variation in the external electric field and a remanent polarization jump at the structural transition. We determined the critical temperature of disappearance of the polarization with the corresponding maximum in the temperature dependences of permittivity and change in the thermopower sign upon temperature variation and the transition from the diffusion of charged particles to the formation of charged regions. In the imaginary component of the impedance, the capacitive contribution prevails.

The sharp maximum and change in a sign of the thermopower

Fig. 9. Temperature dependence of the current in $Bi_2(Sn_{0.85}Cr_{0.15})_2O_7$ measured in zero external electric field at a heating rate of 2 deg/min. Inset: current at $E = 0$ vs reciprocal temperature.

versus temperature was revealed. The hole type of conductivity was determined at high temperature. The qualitative difference between the temperature behaviors of the current in zero electric field and of the thermoelectric current was observed. The prerequisites for the existence of the pyroelectric current in bismuth pyrostannate were established. The growth of remanent polarization of $(Sn_{0.85}Cr_{0.15})_2O_7$ upon heating was interpreted within the model of accumulation of charge carriers at crystallite boundaries.

Acknowledgements

References

[1] D. Janner, D. Tulli, M. Jofre, D. Yudistira, S. Balsamo, M. Belmonte, V. Pruneri, Domain inverted acousto- and electrooptic devices and their application to optical communication, sensing, laser sources, and quantum key distribution, IEEE J. Sel. Top. Quantum Electron 19 (2013) 3400610.

[2] D. Tulli, D. Janner, M. Garcia-Granda, R. Ricken, V. Pruneri, Electrode-free optical sensor for high voltage using a domain-inverted lithium niobate waveguide near cut-off, Appl. Phys. B 103 (2011) 399–403.

[3] B. Bhatia, J. Karthik, T. Tong, David G. Cahill, L.W. Martin, W.P. King, Pyroelectric current measurements on $PbZr_{0.2}Ti_{0.8}O_3$ epitaxial layers, J. Appl. Phys. 112 (2012) 104106.

[4] H.W. Jang, A. Kumar, S. Denev, M.D. Biegalski, P. Maksymovych, C.W. Bark, C.T. Nelson, C.M. Folkman, S.H. Baek, N. Balke, C.M. Brooks, D.A. Tenne, D.G. Schlom, L.Q. Chen, X.Q. Pan, S.V. Kalinin, V. Gopalan, C.B. Eom, Ferroelectricity in strain-free $SrTiO_3$ films, Phys. Rev. Lett. 104 (2010) 197601.

[5] H. Schmid, Multi-ferroic magnetoelectrics, Ferroelectrics 162 (1994) 317–338.

[6] Manfred Fiebig, Thomas Lottermoser, Dennis Meier, Morgan Trassin, The evolution of multiferroics, Nat. Rev. Mater. 1 (2016) 16046, http://dx.doi.org/10.1038/natrevmats.2016.46.

[7] Y. Yamada, K. Kitsuda, S. Nohdo, N. Ikeda, Charge and spin ordering process in the mixed-valence system $LuFe_2O_4$: charge ordering, Phys. Rev. B 62 (2000) 12167.

[8] H.C. Walker, F. Fabrizi, L. Paolasini, F. de Bergevin, J. Herrero-Martin, A.T. Boothroyd, D. Prabhakaran, D.F. McMorrow, Femtoscale magnetically induced lattice distortions in multiferroic $TbMnO_3$, Science 2 (2011) 1273–1276.

[9] SidneyB. Lang, Pyroelectricity: From Ancient Curiosity to Modern Imaging Tool, Physics Today August 31-36, ⟨http://www.physicstoday.org⟩.

[10] Y. Yang, W. Guo, Ken C. Pradel, G. Zhu, Y. Zhou, Y. Zhang, Y. Hu, L. Lin, Z. Lin Wang, Pyroelectric nanogenerators for harvesting thermoelectric energy, Nano Lett. 12 (2012) 2833–2838, http://dx.doi.org/10.1021/nl3003039.

[11] V.A. Isupov, G.I. Golovshchikova, I.E. Mylnikova, Unusual ferroelectric properties of cadmium pyroniobate, Ferroelectrics 8 (1974) 507.

[12] S. Takahashi, Internal bias field effects in lead zirconate-titanate ceramics doped with multiple impurities, Jpn. J. Appl. Phys. 20 (1981) 95–101.

[13] R.S. Roth, J. Res, Pyrochlore-type compounds containing double oxides of trivalent and tetravalent ions, Nat. Bur. Stand. 56 (1956) 17–25.

[14] Ismunandar, Brendan J. Kennedy, Brett A. Hunter, Tom Vogt, Bonding and structural variations in Doped $Bi_2Sn_2O_7$, J. Solid State Chem. 131 (1997) 317–325.

[15] G. Vetter, F. Queyroux, J.C. Gilles, Preparation, stability and preliminary crystallographic study on $Bi_2Sn_2O_7$ compound, Mater. Res. Bull. 13 (1978) 211–216.

[16] I. Radosavljevic Evans, J.A.K. Howard, J.S.O. Evans, a-Bi2Sn2O7 – a 176 atom crystal structure from powder diffraction data, J. Mater. Chem. 13 (2003) 2098–2103.

[17] B.J. Kennedy, I.M. Elcombe, Structure and bonding in $Bi_2Sn_2O_7$, Mater. Sci. Forum 278 (1998) 762–767.

[18] R.D. Shannon, J.D. Bierlein, J.L. Gillson, G.A. Jones, A.W. Sleight, Polymorphism in $Bi_2Sn_2O_7$, J. Phys. Chem. Solids 41 (1980) 117–122.

[19] V. Kahlenberg, T. Zeiske, Structure of gamma-$Bi_2Sn_2O_7$ by high temperature powder neutron diffraction, Z. Krist. 212 (1997) 297–301.

[20] R.H. Jones, K.S. Knight, The structure of gamma-$Bi_2Sn_2O_7$ at 725 degrees C by high-resolution neutron diffraction: implications for bismuth(III)-containing pyrochlores, J. Chem. Soc. Dalton (1997) 2551–2555.

[21] Bruker AXS TOPAS V4: General profile and structure analysis software for powder diffraction data, User's Manual. Bruker AXS, Karlsruhe, Germany, 2008.

[22] R.D. Shannon, Revised effective ionic radii and systematic studies of interatomic distances in halides and chalcogenides, Acta Crystallogr. A 32 (1976) 751–767.

[23] S.S. Aplesnin, L.V. Udod, M.N. Sitnikov, N.P. Shestakov, $Bi_2(Sn_{0.95}Cr_{0.05})_2O_7$: structure, IR spectra, and dielectric properties, Ceram. Int. 42 (2016) 5177–5183.

[24] L.V. Udod, S.S. Aplesnin, M.S. Molokeev, Dielectric and electrical properties of polymorphic bismuth pyrostannate $Bi_2Sn_2O_7$, Phys. Solid State 56 (2014) 1315–1319.

[25] N.F. Mott, E.F. Davis, Electronic Processes in Non-Crystalline Materials, Oxford, 1971.

[26] P. Rottländer, M. Hehn, A. Schuhl, Determining the interfacial barrier height and its relation to tunnel magnetoresistance, Phys. Rev. B 65 (2002) 054422.

[27] M. Robert, Hill, Poole-Frenkel conduction in amorphous solids, Philos. Mag. 23 (1971) 59–86.

[28] G.B. Abdullaev, O.B. Tagiev, G.M. Niftiev, T.Kh Azizov, Injection and thermo-activation currents in $EuGa_2S_4$ single crystals, Phys. Status Solidi (a) 71 (1982) k45–k48.

[29] J.R. Macdonald, Impedance spectroscopy: old problems and new developments, Electrochim. Acta 35 (1990) 1483–1492.

[30] A. Doi, Comment on Warburg impedance and related phenomena, Solid State Ion. 40–41 (1990) 262–265.

[31] V.V. Nikonenko, A.E. Kozmai, Electrical equivalent circuit of an ion-exchange membrane system, Electrochim. Acta 56 (2011) 1262–1269.

[32] Rafael M. Almeida, Carlos William A. Paschoal, Jeffrey T. Auletta, Zachary R. Kann, Michael W. Lufaso, Ionic conductivity in $Bi_2Sn_2O_7$ ceramics, Ceram. Int. 38 (2012) 1275–1279.

[33] S.S. Aplesnin, L.V. Udod, M.N. Sitnikov, E.V. Eremin, M.S. Molokeev, L.S. Tarasova, K.I. Yanushkevich, A.I. Galyas, Correlation of magnetic and transport properties with polymorphic transitions in bismuth pyrostannate $Bi_2(Sn_{1-x}Cr_x)_2O_7$, Phys. Solid State 57 (2015) 1627–1632.

[34] Y. Gelbstein, J. Tunbridge, R. Dixon, M.J. Reece, H.P. Ning, R. Gilchrist, R. Summers, I. Agote, M.A. Lagos, K. Simpson, C. Rouaud, P. Feulner, S. Rivera, R. Torrecillas, M. Husband, J. Crossley, I. Robinson, Physical, mechanical and structural properties of highly efficient nanostructured n- and p- silicides for practical thermoelectric applications, J. Electron. Mater. 43 (2014) 1703–1711.

[35] O. Appel, M. Schwall, M. Kohne, B. Balke, Y. Gelbstein, Effects of microstructural evolution effects on the thermoelectric properties of spark plasma sintered $Ti_{0.3}Zr_{0.35}Hf_{0.35}NiSn$ half-Heusler compound, J. Electron. Mater. 42 (2013) 1340–1345.

[36] O. Appel, T. Zilber, S. Kalabukhov, O. Beeri, Y. Gelbstein, Morpholoical effects on the thermoelectric properties of $Ti_{0.3}Zr_{0.35}Hf_{0.35}Ni_{1+δ}Sn$ alloys following phase separation, J. Mater. Chem. C 3 (2015) 11653–11659.

[37] Roi Vizel, Tal Bargig, Ofer Beeri, Yaniv Gelbstein, Bonding of Bi_2Te_3 based thermoelectric legs to metallic contacts using $Bi_{0.82}Sb_{0.18}$ alloy, J. Electron. Mater. 45 (2016) 1296–1300.

[38] Yaniv Gelbstein, $Pb_{1-x}Sn_xTe$ alloys - application considerations, J. Electron. Mater. 40 (2011) 533–536.

[39] Yaniv Gelbstein, Phase morphology effects on the thermoelectric properties of $Pb_{0.25}Sn_{0.25}Ge_{0.5}Te$, Acta Mater. 61 (2013) 1499–1507 (2013).

[40] Boaz Dado, Yaniv Gelbstein, Dimitri Mogilansky, Vladimir Ezersky, Moshe P. Dariel, Structural evolution following spinodal decomposition of the pseudo-ternary compound $(Pb_{0.3}Sn_{0.1}Ge_{0.6})Te$, J. Electron. Mater. 39 (2010) 2165–2171.

[41] E. Hazan, O. Ben-Yehuda, N. Madar, Y. Gelbstein, Functional graded germanium-lead chalcogenides- based thermoelectric module for renewable energy applications, Adv. Energy Mater. 5 (2015) 1500272.